International Journal of Multiphase Flow 188 (2025) 105200

Contents lists available at ScienceDirect

International Journal of Multiphase Flow

journal homepage: www.elsevier.com/locate/ijmulflow

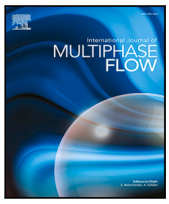

Research Paper

An immersed boundary method for particle-resolved simulations of arbitrary-shaped rigid particles

Maximilian Schenk [a], Manuel García-Villalba [a], Jan Dušek [b], Markus Uhlmann [c], Manuel Moriche [a,*]

[a] Institute of Fluid Mechanics and Heat Transfer, TU Wien, Vienna, Austria
[b] Université de Strasbourg, Department of Mechanics, Institut ICube, Strasbourg, France
[c] Institute for Water and Environment, Karlsruhe Institute of Technology, Karlsruhe, Germany

ARTICLE INFO

Keywords:
Immersed Boundary Method
Neutrally-buoyant particles
Spectral element method
Benchmark
Non-spherical particles

ABSTRACT

The present work extends the direct-forcing immersed boundary method introduced by García-Villalba et al. (2023), broadening its application from spherical to arbitrarily-shaped particles, while maintaining its capacity to address both neutrally-buoyant and light objects (down to a density ratio of 0.5). The proposed method offers a significant advantage over existing methods regarding its simplicity, in particular for the case of neutrally-buoyant particles. Three test cases from the literature are selected for validation: a neutrally-buoyant prolate spheroid in a shear flow; a settling oblate spheroid; and, finally, a rising oblate spheroid.

1. Introduction

Particle-laden flows are commonly found in the environment, such as microplastic pollution in the ocean or snow avalanches, as well as in engineered systems like chemical reactors and fluidized beds. These flows are governed by the complex interaction between fluid and particle motion, and for small particles in dilute conditions, point-particle models can accurately predict the behavior of particles in the flow. However, when the size of the particles is comparable to (or larger than) that of the smaller scales of the flow, and/or the concentration of particles is not small, the predictive capability of the point-particle approach is still low, and one needs to resort to particle-resolved (PR) simulations. Among the several available techniques (Uhlmann et al., 2023), the Immersed Boundary Method (IBM) has gained popularity for PR simulations of particle-laden flows because of its computational efficiency, versatility and accuracy (Mittal and Iaccarino, 2005; Verzicco, 2023).

The IBM was first developed by Peskin (1972) for heart flow simulations. Since then, it has been expanded to tackle a broad spectrum of problems (Griffith and Patankar, 2020; Mittal and Bhardwaj, 2021; Arranz et al., 2022). Unlike methods with a boundary-conforming mesh, which require complex mesh adaptations to account for moving or flexible bodies, IBM simplifies the process by allowing bodies to be treated with a fixed computational grid. Sotiropoulos and Yang (2014) and Mittal and Seo (2023) present a comprehensive review of the available IBM approaches, among them, a widely used method is the direct-forcing method of Uhlmann (2005) due to its computational efficiency, proven accuracy and ease of implementation. However, in Uhlmann's method, stability considerations lead to a lower limit for the density ratio between the solid and fluid phases of approximately 1.2. Several approaches have been taken to overcome this problem. Kempe and Fröhlich (2012) and Breugem (2012) independently worked on the forcing scheme, each improving numerical stability and enabling simulations with a solid/fluid density ratio greater than 0.3. Schwarz et al. (2016) further modified the approach of Kempe and Fröhlich (2012) by introducing the virtual mass method, adding a stabilizing term to both sides of the Newton–Euler equations. Another modification to the method of Kempe and Fröhlich (2012) was proposed by Tschisgale et al. (2017, 2018). The most important modification with respect to the original method of Uhlmann is a different coupling between the fluid and solid equations. In addition, the method relies on using a surface layer of mass and, as a consequence, for non-spherical bodies, additional terms are required in the equations to handle the possible non-overlapping between the centers of mass of the particle and the surface layer. Recently, García-Villalba et al. (2023) proposed a modification to the direct-forcing method described in Uhlmann (2005) by incorporating some of the concepts of the solid–fluid coupling from Tschisgale et al. (2017). The method proposed by García-Villalba et al. (2023) shows no instability for neutrally-buoyant and even moderately-light particles (with density ratio larger than 0.5), keeping the spirit of Uhlmann's method regarding its simplicity.

* Corresponding author.
E-mail address: manuel.moriche@tuwien.ac.at (M. Moriche).

https://doi.org/10.1016/j.ijmultiphaseflow.2025.105200
Received 3 December 2024; Received in revised form 15 February 2025; Accepted 26 February 2025
Available online 9 March 2025

In this paper, we extend the method described by García-Villalba et al. (2023), which focuses solely on spheres, to handle non-spherical particles of arbitrary shape while maintaining the advantages of being able to deal with neutrally-buoyant and moderately-light objects. The simplicity of the proposed methodology stands out as a substantial advantage, as it eliminates the need for any extra terms related to the possible non-overlap between the particle's center of gravity and its surface shell as in Tschisgale et al. (2017, 2018). The simplicity of the formulation is especially evident in the case of neutrally-buoyant particles, as will be shown below. However, the applicability of the methodology is somewhat lower, being limited for stability considerations to particles with a density ratio larger than 0.5 as already discussed by García-Villalba et al. (2023).

The paper is organized as follows. The governing equations and the coupling between the fluid and solid phases are provided in Section 2 together with the full description of the flow solver and the spatial discretization. In Section 3 we present a set of validation cases: (i) a neutrally-buoyant prolate spheroid in shear flow, (ii) a settling oblate spheroid in an unbounded domain and (iii) a light ascending oblate spheroid in an unbounded domain. The paper concludes with final remarks in Section 4.

2. Methodology

We consider the interaction between particles of arbitrary shape and uniform density distribution, ρ_p, with a Newtonian fluid of constant kinematic viscosity, ν, and constant density, ρ_f. Further, we assume the flow to be incompressible and the particles to be rigid bodies. We extend the method proposed by García-Villalba et al. (2023) to handle particles of arbitrary shape by (i) tracking the rotation of the particles employing a quaternion-based formulation and (ii) solving the angular momentum equation of the particle in a body-fixed reference frame, similar to Moriche et al. (2021).

2.1. Governing equations

The Navier–Stokes equations for an incompressible flow read

$$\nabla \cdot \boldsymbol{u} = 0, \tag{1}$$

$$\frac{\partial \boldsymbol{u}}{\partial t} + (\boldsymbol{u}\cdot\nabla)\,\boldsymbol{u} = -\nabla p + \nu\nabla^2\boldsymbol{u} + \boldsymbol{f}, \tag{2}$$

where $\boldsymbol{u}$ is the fluid velocity, p is the kinematic pressure (*i.e.* pressure divided by fluid density) and $\boldsymbol{f}$ is a volume force term which represents the presence of a body (in our case a particle). The volume force $\boldsymbol{f}$ is formulated as a coupling force to impose the no-slip, no-penetration boundary condition on the surface of the particle. Consistent with the original method proposed by Uhlmann (2005), the equations are applied over the entire domain, Ω, including the fluid, Ω_f, and the space occupied by the particle, S.

Particle motion is driven by hydrodynamic and buoyancy forces, thus it is governed by the Newton–Euler equations with the corresponding terms

$$\rho_p V_p \frac{\mathrm{d}\boldsymbol{u}_p}{\mathrm{d}t} = \rho_f \oint_{\partial S} \boldsymbol{\tau}\cdot\boldsymbol{n}\,\mathrm{d}\sigma + \left(\rho_p - \rho_f\right) V_p \mathbf{g}, \tag{3}$$

$$\frac{\mathrm{d}\mathbf{H}_p}{\mathrm{d}t} = \rho_f \oint_{\partial S} \boldsymbol{r}\times(\boldsymbol{\tau}\cdot\boldsymbol{n})\,\mathrm{d}\sigma, \tag{4}$$

where V_p is the volume of the particle, $\boldsymbol{u_p} = (u_{px}, u_{py}, u_{pz})$ is the velocity of its center of mass, $\boldsymbol{\tau} = -p\boldsymbol{I} + \nu\left(\nabla\boldsymbol{u} + \nabla\boldsymbol{u}^T\right)$ is the hydrodynamic stress tensor ($\boldsymbol{I}$ is the identity tensor), $\boldsymbol{n}$ is the unit normal vector pointing towards the fluid, and $\boldsymbol{g}$ is the gravitational acceleration. Further, we define the angular momentum of the particle with respect to the center of mass $\boldsymbol{H}_p = \boldsymbol{I}_p\boldsymbol{\omega}_p^T$ from the inertia tensor of the particle, $\boldsymbol{I}_p$, and the angular velocity, $\boldsymbol{\omega}_p = (\omega_{px}, \omega_{py}, \omega_{pz})$, and the position vector $\boldsymbol{r} = \boldsymbol{x} - \boldsymbol{x_p}$ of any point in the body, $\boldsymbol{x}$, relative to the center of mass, $\boldsymbol{x}_p$. The surface integrals in (3) and (4) can be related to the forcing term through Cauchy's principle (Uhlmann, 2005, see, Appendix B) as shown below

$$\oint_{\partial S} \boldsymbol{\tau}\cdot\boldsymbol{n}\mathrm{d}\sigma = -\int_S \boldsymbol{f}\,\mathrm{d}\boldsymbol{x} + \frac{\mathrm{d}}{\mathrm{d}t}\int_S \boldsymbol{u}\,\mathrm{d}\boldsymbol{x}, \tag{5}$$

$$\oint_{\partial S} \boldsymbol{r}\times(\boldsymbol{\tau}\cdot\boldsymbol{n})\,\mathrm{d}\sigma = -\int_S (\boldsymbol{r}\times\boldsymbol{f})\,\mathrm{d}\boldsymbol{x} + \frac{\mathrm{d}}{\mathrm{d}t}\int_S (\boldsymbol{r}\times\boldsymbol{u})\,\mathrm{d}\boldsymbol{x}. \tag{6}$$

The second term of the right-hand side of (5) can be expressed as

$$\frac{\mathrm{d}}{\mathrm{d}t}\int_S \boldsymbol{u}\,\mathrm{d}\boldsymbol{x} = V_p\frac{\mathrm{d}\boldsymbol{u}_p}{\mathrm{d}t}, \tag{7}$$

and further assuming that the flow inside of the particle follows its rigid-body motion, we can express the second term in the right-hand side of (6) as

$$\frac{\mathrm{d}}{\mathrm{d}t}\int_S (\boldsymbol{r}\times\boldsymbol{u})\,\mathrm{d}\boldsymbol{x} = \frac{1}{\rho_p}\frac{\mathrm{d}\mathbf{H}_p}{\mathrm{d}t}. \tag{8}$$

Considering all the assumptions detailed above, Eqs. (3) and (4) can be rewritten as

$$\left(1-\frac{\rho_f}{\rho_p}\right)V_p\frac{\mathrm{d}\boldsymbol{u}_p}{\mathrm{d}t} = -\frac{\rho_f}{\rho_p}\int_S \boldsymbol{f}\,\mathrm{d}\boldsymbol{x} + \left(1-\frac{\rho_f}{\rho_p}\right)V_p\mathbf{g}, \tag{9}$$

$$\left(1-\frac{\rho_f}{\rho_p}\right)\frac{\mathrm{d}\mathbf{H}_p}{\mathrm{d}t} = -\rho_f\int_S (\boldsymbol{r}\times\boldsymbol{f})\,\mathrm{d}\boldsymbol{x}. \tag{10}$$

2.2. Coupling condition

Following García-Villalba et al. (2023), we combine the convective, pressure and viscous terms from Eq. (2) into the variable $\boldsymbol{rhs}$

$$\boldsymbol{f} = \frac{\partial\boldsymbol{u}}{\partial t} - \boldsymbol{rhs}, \tag{11}$$

and integrate Eq. (11) in time as originally proposed by Tschisgale et al. (2017)

$$\int_{t_{n-1}}^{t_n}\boldsymbol{f}\,\mathrm{d}t = \int_{t_{n-1}}^{t_n}\left(\frac{\partial\boldsymbol{u}}{\partial t} - \boldsymbol{rhs}\right)\mathrm{d}t = \boldsymbol{u}^n - \boldsymbol{u}^{n-1} - \int_{t_{n-1}}^{t_n}\boldsymbol{rhs}\,\mathrm{d}t, \tag{12}$$

where $\boldsymbol{u}^n$ is the fluid velocity at the time instant t_n. Eq. (12) can be rewritten as

$$\int_{t_{n-1}}^{t_n}\boldsymbol{f}\,\mathrm{d}t = \boldsymbol{u}^n - \tilde{\boldsymbol{u}} \quad \forall\boldsymbol{x}\in S, \tag{13}$$

where $\tilde{\boldsymbol{u}}$ is an estimated velocity obtained explicitly without considering the presence of the body, hence ignoring the forcing term $\boldsymbol{f}$

$$\tilde{\boldsymbol{u}} = \boldsymbol{u}^{n-1} + \int_{t_{n-1}}^{t_n}\boldsymbol{rhs}\,\mathrm{d}t. \tag{14}$$

Under the rigid-body assumption, the particle velocity and the fluid velocity at any interior point at the end of the interval (t^n) are related through

$$\boldsymbol{u}^n = \boldsymbol{u}_p^n + \boldsymbol{\omega}_p^n\times\boldsymbol{r}^n \quad \forall\boldsymbol{x}\in S. \tag{15}$$

Integrating the solid-phase equations, (9) and (10), over the time interval $[t_{n-1}, t_n]$ results in

$$\left(1-\frac{\rho_f}{\rho_p}\right)V_p\left(\boldsymbol{u}_p^n - \boldsymbol{u}_p^{n-1}\right) = -\frac{\rho_f}{\rho_p}\int_S\int_{t_{n-1}}^{t_n}\boldsymbol{f}\,\mathrm{d}t\mathrm{d}\boldsymbol{x} + \left(1-\Delta t\frac{\rho_f}{\rho_p}\right)V_p\mathbf{g}, \tag{16}$$

$$\left(1-\frac{\rho_f}{\rho_p}\right)\left(\boldsymbol{H}_p^n - \boldsymbol{H}_p^{n-1}\right) = -\rho_f\int_S\int_{t_{n-1}}^{t_n}(\boldsymbol{r}\times\boldsymbol{f})\,\mathrm{d}t\,\mathrm{d}\boldsymbol{x}, \tag{17}$$

where $\Delta t = t_n - t_{n-1}$. An additional benefit of the present methodology is linked to the exact temporal integration of Eq. (10) leading to Eq. (17). As we do not need to compute the time derivative of $\boldsymbol{H}_p$, then we do not need to deal with the cross-term $\boldsymbol{\omega}_p\times\boldsymbol{H}_p$ that appears when taking time derivates in non-inertial reference frames. The treatment of Eq. (17) is simplified by using a body-fixed reference frame, so that the inertia tensor is constant. In addition, the axes of the body-fixed reference frame are aligned with the principal axes of inertia of the body, leading

to a diagonal inertia tensor. These two steps are not a requirement of the method and could be performed differently if needed for some particular reason. The right-hand side of Eq. (17) is available in the laboratory frame, so that it needs to be expressed in the body-fixed frame by using the rotation matrix, $\mathcal{R}$, of the previous step. This is because the new orientation of the body is not yet known (Moriche et al., 2021). More specifically, we define the rotation matrix as a function of the particle orientation in terms of the quaternion $\mathbf{q}$ as follows:

$$\mathcal{R}^n = \mathcal{R}(\mathbf{q}^n), \tag{18}$$

where the entries in the matrix $\mathcal{R}$ are given in (56). Hence, the angular momentum equation in a body-fixed reference frame can be written as:

$$\left(1-\frac{\rho_f}{\rho_p}\right)\boldsymbol{I}_{p,b}\left(\boldsymbol{\omega}_{p,b}^{n}-\boldsymbol{\omega}_{p,b}^{n-1}\right) = -\rho_f\mathcal{R}^{n-1}\left[\int_S\int_{t_{n-1}}^{t_n}(\boldsymbol{r}\times\boldsymbol{f})\,\mathrm{d}t\,\mathrm{d}\boldsymbol{x}\right], \tag{19}$$

where the subscript b stands for the body-fixed reference frame.

Next, we follow Tschisgale et al. (2017) to express the double integrals on the right-hand side of Eqs. (16) and (19) in terms of the particle kinematics at the end of the interval and of the preliminary velocity

$$\int_S\int_{t_{n-1}}^{t_n}\boldsymbol{f}\,\mathrm{d}t\,\mathrm{d}\boldsymbol{x} = \int_S(\boldsymbol{u}_p^n+\boldsymbol{\omega}_p^n\times\boldsymbol{r}-\tilde{\boldsymbol{u}})\mathrm{d}\boldsymbol{x} = V_p\boldsymbol{u}_p^n-\int_S\tilde{\boldsymbol{u}}\,\mathrm{d}\boldsymbol{x}, \tag{20}$$

$$\int_S\int_{t_{n-1}}^{t_n}(\boldsymbol{r}\times\boldsymbol{f})\mathrm{d}t\,\mathrm{d}\boldsymbol{x} = \int_S\left[\boldsymbol{r}\times(\boldsymbol{u}_p^n+\boldsymbol{\omega}_p^n\times\boldsymbol{r}-\tilde{\boldsymbol{u}})\right]\mathrm{d}\boldsymbol{x} = \frac{\boldsymbol{I}_p}{\rho_p}\boldsymbol{\omega}_p^n-\int_S\boldsymbol{r}\times\tilde{\boldsymbol{u}}\,\mathrm{d}\boldsymbol{x}. \tag{21}$$

Combining the last steps by substituting Eqs. (20)–(21) into Eqs. (16) and (19) and rearranging, we obtain

$$\boldsymbol{u}_p^n = \left(1-\frac{\rho_f}{\rho_p}\right)\boldsymbol{u}_p^{n-1}+\frac{1}{V_p}\frac{\rho_f}{\rho_p}\int_S\tilde{\boldsymbol{u}}\,\mathrm{d}\boldsymbol{x}+\Delta t\left(1-\frac{\rho_f}{\rho_p}\right)\boldsymbol{g}, \tag{22}$$

$$\boldsymbol{\omega}_{p,b}^n = \left(1-\frac{\rho_f}{\rho_p}\right)\boldsymbol{\omega}_{p,b}^{n-1}+\boldsymbol{I}_{p,b}^{-1}\rho_f\mathcal{R}^{n-1}\left[\int_S\boldsymbol{r}\times\tilde{\boldsymbol{u}}\,\mathrm{d}\boldsymbol{x}\right]. \tag{23}$$

The studies by Yu and Shao (2007) and Moriche et al. (2021) show that forcing throughout the volume enclosed by the particle, S, is superior to forcing only on its surface, ∂S, since it leads to a velocity field that fulfills the rigid-body assumption more closely. Furthermore, if the distribution of Lagrangian markers throughout the volume is sufficiently uniform and homogeneous, the integrals in (22) and (23) can be approximated to second-order accuracy by using discrete sums, as numerically verified by García-Villalba et al. (2023). We use this fact as an opportunity to apply forcing inside the particle at practically no additional cost in the interpolation step of the IBM (please refer to B for an analysis of the computational costs of surface- and volume-forcing approaches, and the implications that these IBM-related costs would have when considering many particles). Considering the above, the two integrals in (22) and (23) can be readily approximated using discrete sums

$$\int_S\tilde{\boldsymbol{u}}\,\mathrm{d}\boldsymbol{x} \approx \sum_{l=1}^{N_l}\tilde{\boldsymbol{U}}_l\Delta V_l, \tag{24}$$

$$\int_S\boldsymbol{r}\times\tilde{\boldsymbol{u}}\,\mathrm{d}\boldsymbol{x} \approx \sum_{l=1}^{N_l}\boldsymbol{R}(\boldsymbol{X}_l)\times\tilde{\boldsymbol{U}}_l\Delta V_l, \tag{25}$$

where ΔV_l and $\boldsymbol{R}(\boldsymbol{X}_l)=\boldsymbol{X}_l-\boldsymbol{x}_p$ are the discrete volume and the position relative to the particle center, respectively, of the lth Lagrangian marker, and $\tilde{\boldsymbol{U}}_l$ denotes the preliminary velocity of the lth marker, that will be used later to compute the forcing term. Substituting the discrete sums into Eqs. (22) and (23), we finally obtain

$$\boldsymbol{u}_p^n = \left(1-\frac{\rho_f}{\rho_p}\right)\boldsymbol{u}_p^{n-1}+\frac{1}{V_p}\frac{\rho_f}{\rho_p}\sum_{l=1}^{N_l}\tilde{\boldsymbol{U}}_l\Delta V_l+\Delta t\left(1-\frac{\rho_f}{\rho_p}\right)\boldsymbol{g}, \tag{26}$$

$$\boldsymbol{\omega}_{p,b}^n = \left(1-\frac{\rho_f}{\rho_p}\right)\boldsymbol{\omega}_{p,b}^{n-1}+\boldsymbol{I}_{p,b}^{-1}\rho_f\mathcal{R}^{n-1}\left[\sum_{l=1}^{N_l}\left(\boldsymbol{R}(\boldsymbol{X}_l)\times\tilde{\boldsymbol{U}}_l\right)\Delta V_l\right]. \tag{27}$$

The velocity updates shown in Eqs. (26) and (27) exhibit the same stability properties as in García-Villalba et al. (2023), *i.e.* they are unstable for $\rho_p/\rho_f \le 0.5$.

Finally, for the case of neutrally-buoyant particles ($\rho_p/\rho_f = 1$), Eqs. (26)–(27) are reduced to

$$\boldsymbol{u}_p^n = \frac{1}{V_p}\sum_{l=1}^{N_l}\tilde{\boldsymbol{U}}_l\Delta V_l, \tag{28}$$

$$\boldsymbol{\omega}_{p,b}^n = \boldsymbol{I}_{p,b}^{-1}\rho_f\mathcal{R}^{n-1}\left[\sum_{l=1}^{N_l}\left(\boldsymbol{R}(\boldsymbol{X}_l)\times\tilde{\boldsymbol{U}}_l\right)\Delta V_l\right]. \tag{29}$$

2.3. Flow solver and spatial discretization

We solve the governing equations in a similar way as in the original method proposed by Uhlmann (2005), except for the use of the extended fluid-solid coupling technique, which is described in detail in Section 2.2. To ensure continuity, we solve Eqs. (1) and (2) by means of a projection method (Brown et al., 2001). Spatial discretization is done with second-order finite differences on a staggered, uniform grid and time marching is performed with a low-storage semi-implicit three-stage Runge–Kutta scheme, where linear terms are treated implicitly, and non-linear terms explicitly. Denoted as $\boldsymbol{x}_{ijk}^{\beta}$, the grid points' positions refer to the staggered grid associated with the velocity component u_β, where β takes values of 1, 2 and 3.

Lagrangian quantities are represented by uppercase letters. To uniformly distribute N_L points throughout the volume of a non-spherical particle, we generate a 3D Voronoï tessellation and use Lloyd's algorithm (Lloyd, 1982) to iterate their coordinates until we achieve convergence. These positions are represented as $\boldsymbol{X}_l \forall S$, with $1 \le l \le N_L$. A discrete volume ΔV_l is assigned to each point so that the particle's total volume is the sum of these discrete volumes. The procedure for obtaining the distribution of points is illustrated in Moriche et al. (2021).

Quantities are transferred between Lagrangian and Eulerian grids using the regularized delta function, δ_h, as described in Peskin (2002) and defined in Roma et al. (1999). For the kth Runge–Kutta stage, we first compute the preliminary velocity $\tilde{\boldsymbol{u}}$ by advancing the momentum equation ignoring the presence of the particle and without considering the continuity constraint

$$\tilde{\boldsymbol{u}} = \boldsymbol{u}^{k-1}+\Delta t\left(2\alpha_k\nu\nabla^2\boldsymbol{u}^{k-1}-2\alpha_k\nabla p^{k-1}-\gamma_k\left((\boldsymbol{u}\cdot\nabla)\boldsymbol{u}\right)^{k-1}-\xi_k\left((\boldsymbol{u}\cdot\nabla)\boldsymbol{u}\right)^{k-2}\right), \tag{30}$$

where the coefficients α_k, γ_k, ξ_k ($1 \le k \le 3$) are those used by Rai and Moin (1991). Afterwards, the preliminary velocity is transferred from the Eulerian to the Lagrangian grid

$$\tilde{U}_{\beta,l} = \sum_{ijk}\tilde{u}_\beta(\boldsymbol{x}_{ijk}^{\beta})\delta_h\left(\boldsymbol{x}_{ijk}^{\beta}-\boldsymbol{X}_l^{k-1}\right)\Delta x^3, \quad \forall l; 1 \le \beta \le 3. \tag{31}$$

In the original method by Uhlmann (2005), the subsequent step is computing the force volume term using the particle velocity of the previous stage $k-1$. Instead, in the current method, the next step is to compute the present particle velocity, $\boldsymbol{u}_p^k$, and the present angular velocity of the particle, $\boldsymbol{\omega}_{p,b}^k$, computed in the body-fixed reference frame

$$\boldsymbol{u}_p^k = \left(1-\frac{\rho_f}{\rho_p}\right)\boldsymbol{u}_p^{k-1}+\frac{1}{V_p}\frac{\rho_f}{\rho_p}\sum_{l=1}^{N_l}\tilde{\boldsymbol{U}}_l\Delta V_l+2\alpha_k\Delta t\left(1-\frac{\rho_f}{\rho_p}\right)\boldsymbol{g}, \tag{32}$$

$$\boldsymbol{\omega}_{p,b}^k = \left(1-\frac{\rho_f}{\rho_p}\right)\boldsymbol{\omega}_{p,b}^{k-1}+\boldsymbol{I}_{p,b}^{-1}\rho_f\mathcal{R}^{k-1}\left(\sum_{l=1}^{N_l}\boldsymbol{R}(\boldsymbol{X}_l^{k-1})\times\tilde{\boldsymbol{U}}_l\Delta V_l\right). \tag{33}$$

The appearance of $2\alpha_k$ in Eq. (32) is due to the derivation of Eq. (26) using a generic time step Δt, whereas the time step associated with the k-th stage is $2\alpha_k\Delta t$. For a neutrally-buoyant case, we can replace these

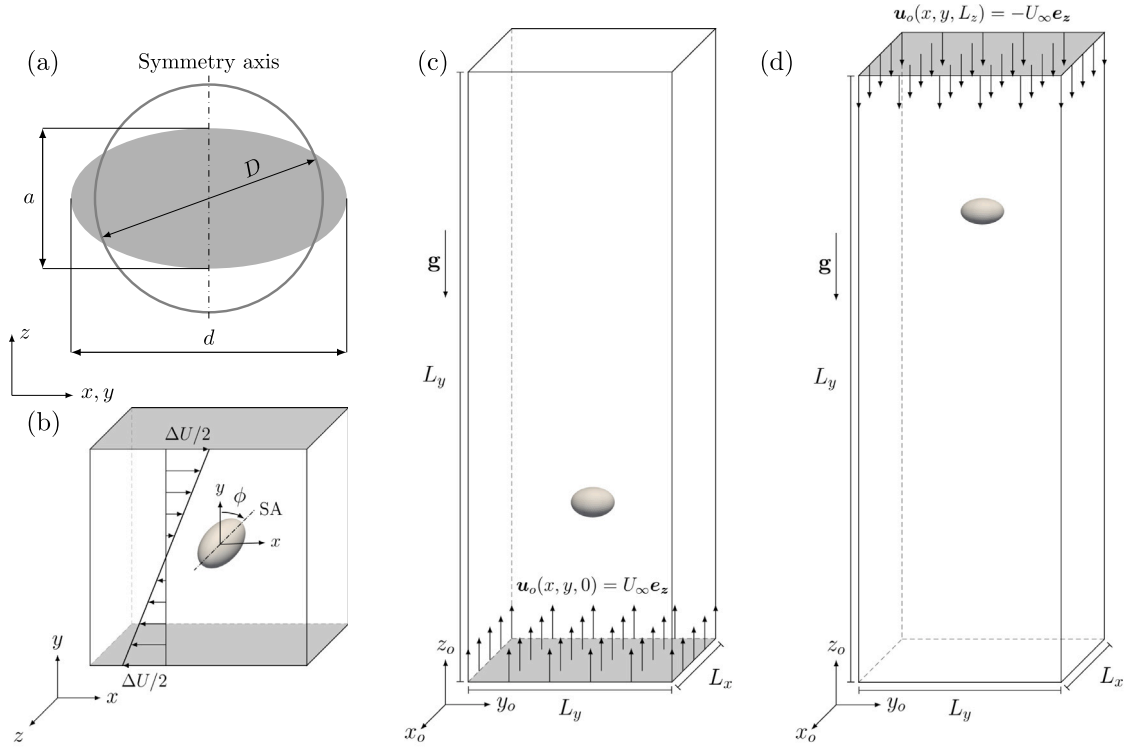

Fig. 1. (a) Sketch of a spheroid with $\chi = d/a = 2$ and equivalent sphere $D = d/\chi^{1/3}$. (b) Computational setup for neutrally-buoyant prolate spheroid in shear flow with a visual representation of the angle, ϕ. Sketch of the computational set-up for (c) settling and (d) rising particles.

equations with

$$\boldsymbol{u}_p^k = \frac{1}{V_p}\frac{\rho_f}{\rho_p}\sum_{l=1}^{N_l}\tilde{\boldsymbol{U}}_l \Delta V_l\,, \tag{34}$$

$$\boldsymbol{\omega}_{p,b}^k = \boldsymbol{I}_{p,b}^{-1}\rho_f \mathcal{R}^{k-1}\left(\sum_{l=1}^{N_l}\boldsymbol{R}(\boldsymbol{X}_l^{k-1})\times\tilde{\boldsymbol{U}}_l\Delta V_l\right). \tag{35}$$

Using these velocities of the rigid body, we can now determine the new desired velocity

$$\boldsymbol{U}_l^{(d)} = \boldsymbol{u}_p^k + \left(\mathcal{R}^{k-1}\right)^T\left(\boldsymbol{\omega}_{p,b}^k \times \boldsymbol{R}(\boldsymbol{X}_{l,b})\right) \quad \forall l\,. \tag{36}$$

Please note that in (36) the rotation matrix is computed with the quaternion from the previous Runge–Kutta stage. Following this, the subsequent steps of the original fluid phase method from Uhlmann (2005) remain unchanged. As a result, the following operations can be performed in sequence:

$$\boldsymbol{F}_l = \frac{\boldsymbol{U}_l^{(d)} - \tilde{\boldsymbol{U}}_l}{\Delta t} \quad \forall l\,, \tag{37}$$

$$f_\beta^k(\boldsymbol{x}_{ijk}^\beta) = \sum_{l=1}^{N_l} F_{\beta,l}\delta_h(\boldsymbol{x}_{ijk}^\beta - \boldsymbol{X}_l^{k-1})\Delta V_l \quad \forall i,j,k; 1\le\beta\le 3\,, \tag{38}$$

$$\nabla^2\boldsymbol{u}^* - \frac{\boldsymbol{u}^*}{\alpha_k \Delta t \nu} = -\frac{1}{\alpha_k \nu}\left(\frac{\tilde{\boldsymbol{u}}}{\Delta t} + \boldsymbol{f}^k\right) + \nabla^2\boldsymbol{u}^{k-1}\,, \tag{39}$$

$$\nabla^2\phi = \frac{\nabla\cdot\boldsymbol{u}^*}{2\alpha_k\Delta t}\,, \tag{40}$$

$$\boldsymbol{u}^k = \boldsymbol{u}^* - 2\alpha_k\Delta t\nabla\phi\,, \tag{41}$$

$$p^k = p^{k-1} + \phi - \alpha_k\Delta t\nu\nabla^2\phi\,, \tag{42}$$

where ϕ is the pseudo-pressure. Then, we determine the new position of the particle's center of mass, $\boldsymbol{x}_p^k$, update the quaternions, $\boldsymbol{q}^k$, and also update the rotation matrix, $\mathcal{R}^k = \mathcal{R}(\boldsymbol{q}^k)$, which is defined in A along with the matrix $\mathbf{Q}^k = \mathbf{Q}(\boldsymbol{\omega}_{p,b}^k)$.

$$\boldsymbol{x}_p^k = \boldsymbol{x}_p^{k-1} + \alpha_k\Delta t\left(\boldsymbol{u}_p^k + \boldsymbol{u}_p^{k-1}\right), \tag{43}$$

$$\frac{\tilde{\boldsymbol{q}}^k - \boldsymbol{q}^{k-1}}{\Delta t} = \gamma_k\frac{1}{2}\boldsymbol{Q}(\boldsymbol{\omega}_{p,b}^{k-1})\boldsymbol{q}^{k-1} + \xi_k\frac{1}{2}\boldsymbol{Q}(\boldsymbol{\omega}_{p,b}^{k-2})\boldsymbol{q}^{k-2}\,, \tag{44}$$

$$\boldsymbol{q}^k = \frac{\tilde{\boldsymbol{q}}^k}{|\tilde{\boldsymbol{q}}^k|}\,, \tag{45}$$

$$\mathcal{R}^k = \mathcal{R}(\boldsymbol{q}^k)\,, \tag{46}$$

$$\mathbf{Q}^k = \mathbf{Q}(\boldsymbol{\omega}_{p,b}^k)\,. \tag{47}$$

And as a final step, the position of the Lagrangian markers is updated:

$$\boldsymbol{X}_l^k = \boldsymbol{x}_p^k + (\mathcal{R}^k)^T\boldsymbol{R}(\boldsymbol{X}_{l,b})\,. \tag{48}$$

Thus, we conclude the Runge–Kutta stage with this calculation.

3. Validation

In this section, we present the validation of the method proposed above. We have selected distinct scenarios, but in all of them we use particles of spheroidal shape with an aspect ratio $\chi = d/a$ ($\chi < 1$ for prolate spheroids; $\chi > 1$ for oblate spheroids), where d represents the equatorial diameter and a is the symmetry axis length. Additionally, D denotes the equivalent diameter, describing the diameter of a sphere with the same volume (see Fig. 1a). In the absence of an exact solution, we will use for comparison results obtained with a highly-accurate spectral/spectral-element solver (Chrust et al., 2013), as has been done in previous works (Uhlmann and Dusek, 2014; Rettinger and Rüde, 2017; Moriche et al., 2021).

In Section 3.2 and 3.3, the relative errors of converged values are computed for any quantity ϕ as

$$\varepsilon(\phi) = \frac{|\phi - \phi_{ref}|}{\phi_{ref}^*}, \tag{49}$$

where the subscript "ref" denotes a value taken from the reference data. Since some quantities to be compared are of very small amplitude (*e.g.* the horizontal velocity in Table 2),we use an order unity quantity to form ϕ_{ref}^* for the purpose of normalization (*e.g.* the settling particle

Table 1
Parameters and results for the calculations of the neutrally-buoyant prolate spheroid in a shear flow. Errors are computed with respect to the analytical solution by Guazzelli et al. (2012).

Method	$D/\Delta x$	CFL	$T\dot{\gamma}$	ϵ	$\dot{\phi}_{max}$	ϵ	$\dot{\phi}_{min}$	ϵ
Analytical	–	–	15.707	–	0.8	–	0.2	–
IBM	20.0	0.1	16.118	0.0260	0.8114	0.0114	0.1848	0.0152
IBM	20.0	0.01	15.946	0.0152	0.8035	0.0035	0.1925	0.0075
IBM	20.0	0.001	15.842	0.0085	0.7983	0.0016	0.1964	0.0036

velocity, cf. details below and discussion in Uhlmann and Dusek, 2014, p. 234).

3.1. Neutrally buoyant prolate spheroid in shear flow

As a first validation case, we study the rotational behavior of a neutrally-buoyant prolate spheroid in a shear flow. Following Tschisgale et al. (2018), we select a cubic domain of side length $L = 6.4D$ with periodic boundary conditions along the streamwise and spanwise directions (x, z). Dirichlet boundary conditions are imposed at the top and bottom boundaries, namely $(u, v, w) = \pm(\Delta U/2, 0, 0)$ at $y = \pm L/2$. The prolate spheroid has an aspect ratio $\chi = 1/2$. It is initially placed with the center of mass at the center of the computational domain, with its symmetry axis aligned with the y-axis. The density ratio is set to 1, and the kinematic viscosity, ν, and the shear rate $\dot{\gamma} = \Delta U/L$ are adjusted so that $Re_{\dot{\gamma}} = \dot{\gamma} D^2/\nu = 5/32$. Note that the analytical solution is available for Stokes flow ($Re = 0$), while the present calculations are performed at low but finite Re. The calculations are performed using 128^3 grid points, corresponding to a grid resolution of $D/\Delta x = 20$. We initialize the flow with the velocity field $(u(y) = \dot{\gamma} y, v = w = 0)$ that would be the solution in the absence of the particle.

Under Stokes flow conditions, *i.e.* $Re \ll 1$, Jeffery (1922) derived an analytical solution of the problem, known as a Jeffery orbit. This solution is also discussed in detail in Guazzelli et al. (2012). When the symmetry axis of the spheroid is contained in an xy-plane, the rotational motion of the spheroid is periodic and uniquely determined by the angle $\phi(t)$ and its time derivative $\dot{\phi}(t)$. Fig. 1b shows a sketch of the problem and a visual representation of the angle ϕ. Following the notation of Guazzelli et al. (2012) the period is given by

$$T\dot{\gamma} = 2\pi\left(\chi + 1/\chi\right), \tag{50}$$

and the angle of rotation and angular velocity as a function of time are

$$\phi = \arctan\left(\frac{1}{\chi}\tan\left(\frac{\dot{\gamma} t}{\chi + \frac{1}{\chi}}\right)\right), \tag{51}$$

$$\dot{\phi} = \frac{\dot{\gamma}}{1+\chi^2}\left(\chi^2 \sin^2\phi + \cos^2\phi\right). \tag{52}$$

We have performed three simulations varying the time step so that the CFL changes from 0.1 to 0.001 as reported in Table 1. Fig. 2 shows the time evolution of the angular velocity, $\dot{\phi}$. The agreement is very good for the three calculations and the error decreases with decreasing time step, as evident by the insets of the figure in the regions of the local maximum and the local minimum. A quantitative comparison is reported in Table 1, including the period, $T\dot{\gamma}$, and its relative error, along with the maximum and minimum values of the angular velocity, $\dot{\phi}$, and their absolute errors. As the CFL-number decreases, the errors gradually decrease converging to the analytical values, with the possible exception of the local maximum that seems to converge to a value that is slightly below the analytical one. This minor discrepancy may be attributed to the slight differences between the current configuration and the reference solution, namely finite Re and bounded domain.

3.2. Settling spheroid in unbounded domain

Let us now analyze the settling of a single oblate spheroid in an unbounded domain (see Fig. 1c). Dimensional analysis shows that the problem is governed by three non-dimensional parameters, namely the aspect ratio, χ, the density ratio between the particle and the fluid, $\tilde{\rho} = \rho_p/\rho_f$, and the Galileo number $Ga = U_g D/\nu$, where $U_g = \sqrt{|\tilde{\rho} - 1| g D}$ is the gravitationally scaled velocity. We evaluate two different Galileo numbers for a spheroid with $\chi = 1.5$ and $\tilde{\rho} = 2.15$, resulting in two different regimes, namely, the steady-oblique regime and the vertical-periodic regime. As reference we follow the work of Moriche et al. (2021) (referred in the following as MUD21) to compare the present results to results from a spectral/spectral-element method (henceforth called SEM) and from another IBM that employs the original fluid-solid coupling of Uhlmann (2005). As in MUD21, the cuboidal domain has side lengths $L_x = L_y = 6.1D$, a height of $L_z = 18.3D$ and we select grid resolutions with $D/\Delta x = 21$ and $D/\Delta x = 42$. This results in a grid size of $(128 \times 128 \times 384)$ points for the lower resolution and $(256 \times 256 \times 768)$ points for the higher resolution. We impose at the bottom boundary a Dirichlet boundary condition with velocity $\boldsymbol{u}(x, y, 0) = U_\infty \boldsymbol{e}_z$. At the top boundary, we impose an advective boundary condition and periodic boundary conditions are imposed in the lateral directions (x and y). Following the approach used in previous studies (Uhlmann and Dusek, 2014), we adjust the Reynolds number based on U_∞ so that it is as close as possible to the mean settling Reynolds number based on the terminal velocity of the particle, therefore obtaining long integration intervals without incurring high computational costs.

3.2.1. Steady-oblique regime

First, we consider the steady-oblique regime. This regime is ideal for benchmarking because of the simplicity of its resulting kinematics and the narrow range of Ga in which it appears, making it a hard test to reproduce, but to some extent easy to analyze. For the oblate spheroid used here ($\chi = 1.5, \tilde{\rho} = 2.14$) this regime is observed for $Ga \approx [138, 160]$ (see MUD21, Fig. 6). Therefore, we choose $Ga = 152$ and the time-step is adjusted in order to keep the $CFL \approx 0.3$. In this regime, settling particles follow a steady, inclined trajectory, maintaining a constant tilt angle relative to the vertical axis. The angle of the trajectory,

$$\alpha = \arctan\left(\frac{u_{pH}}{u_{pV}}\right), \tag{53}$$

is defined by the non-dimensional vertical velocity, $u_{pV} = u_{pz}/U_g$, and the non-dimensional horizontal velocity, $u_{pH} = \boldsymbol{u}_p \cdot \boldsymbol{e}_{pH}/U_g$, where the unit vector $\boldsymbol{e}_{pH} = (u_{px}, u_{py}, 0)/\sqrt{u_{px}^2 + u_{py}^2}$ indicates the horizontal direction. Interestingly, the tilting angle, ϕ, of the spheroid is not exactly the same as the angle of the trajectory. Therefore, we use this latter angle as an additional measure for validation. Table 2 includes the vertical, u_{pV}, and the horizontal, u_{pH}, velocities, the trajectory angle, α, and the tilting angle, ϕ, obtained with the IBM proposed in this work and the differences/errors with respect to the reference data. Note that MUD21 reports results for IBM simulations where forcing is applied in the entire volume of the particle and IBM simulations where forcing is applied in the surface of the particle. Both are included in the table. The data shows that the proposed method is able to capture this regime adequately. Comparing the results of the current IBM method with the SEM from MUD21, we observe a steady convergence under grid refinement, indicating the reliability of the method. Additionally, we observe that both velocity components and both angles are slightly over-predicted compared to the SEM reference data. Similar trends are

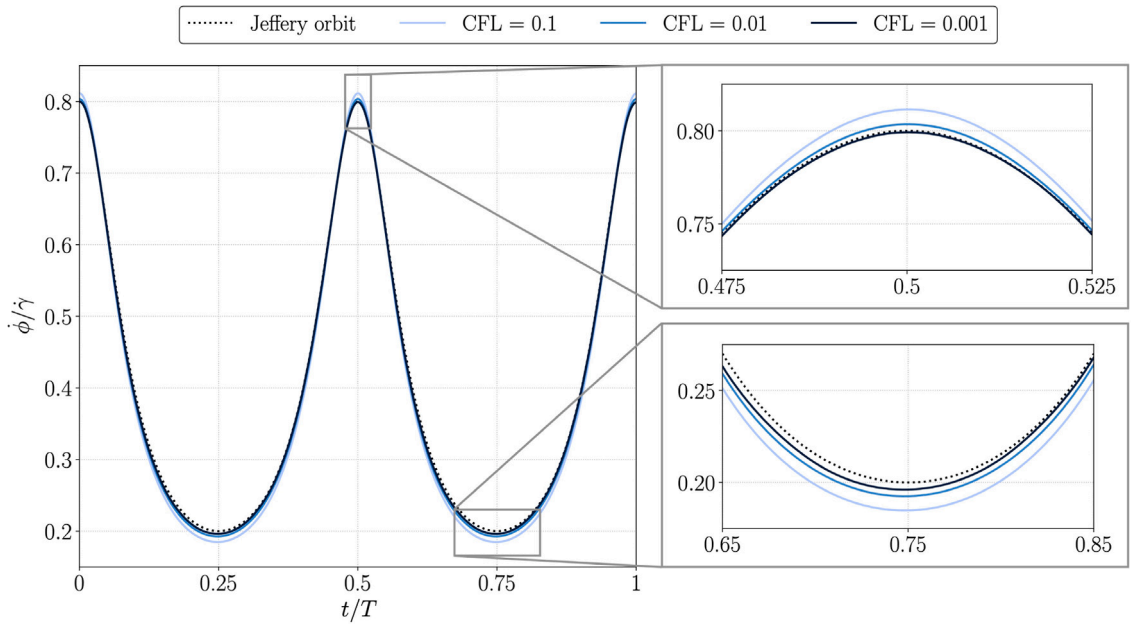

Fig. 2. Time history of ϕ obtained with the proposed method for different CFL-numbers with a resolution of $D/\Delta x = 20$ and the analytical solution for a Jeffery orbit (Guazzelli et al., 2012).

Table 2
Parameters and results for the steady-oblique regime for a settling oblate spheroid. Reference data taken from Moriche et al. (2021). The corresponding SEM values are used for normalization (ϕ^*_{ref} in Eq. (49)), expect for ε_H, where we use $\phi^*_{ref} = u^{\mathrm{SEM}}_{p,V}$.

Method	Work	$\frac{D}{\Delta x}$	Forcing	u_{pV}	ε_V	u_{pH}	ε_H	$\alpha(^\circ)$	ε_α	$\phi(^\circ)$	ε_ϕ
SEM	MUD21 (B15-M075-SEM)	–	–	−1.063	–	0.0714	–	3.842	–	5.318	–
IBM	MUD21 (B15-M075-24)	21	Surface	−1.048	0.0141	0.0616	0.0092	3.364	0.1244	4.676	0.1207
IBM	MUD21 (B15-M075-24-FI)	21	Volume	−1.050	0.0122	0.0735	0.0002	4.004	0.0421	5.710	0.0737
IBM	MUD21 (B15-M075-48)	42	Surface	−1.054	0.0084	0.0657	0.0054	3.566	0.0718	4.890	0.0805
IBM	MUD21 (B15-M075-48-FI)	42	Volume	−1.065	0.0019	0.0757	0.0004	4.066	0.0583	5.600	0.0530
IBM	Current	21	Volume	−1.092	0.0276	0.0793	0.0074	4.164	0.0838	5.687	0.0693
IBM	Current	42	Volume	−1.086	0.0216	0.0781	0.0063	4.111	0.0700	5.674	0.0669

observed for both volume-forcing IBM (-FI) cases from MUD21. Overall, the errors remain within an acceptable range compared to the errors of the IBM results from MUD21.

3.2.2. Vertical-periodic regime

The second regime selected for the settling oblate with $\chi = 1.5$ and $\tilde{\rho} = 2.15$ is unsteady, but periodic. This regime occurs for Ga approximately in the interval $[175, 270]$ (see MUD21, Fig. 6). We select $Ga = 207$ and the time-step is adjusted in order to keep the $CFL \approx 0.5$. The vertical-periodic regime is defined by small lateral oscillations confined to a single plane. As a result, the kinematics reduce to vertical, u_{pV}, and horizontal, u_{pH}, velocity components, and angular velocity, $\omega_{pHz\perp} = \boldsymbol{\omega} \cdot \boldsymbol{e}_{pHz\perp} U_g/D$ ($\boldsymbol{e}_{pHz\perp}$ is the unit vector perpendicular to the vertical, $\boldsymbol{e}_z$, and horizontal, $\boldsymbol{e}_{pH}$, unit vectors). The velocity $u_{pHz\perp} = \boldsymbol{u}_p \cdot \boldsymbol{e}_{pHz\perp}/U_g$ indicates whether the motion occurs solely within one plane, and therefore, it should be zero in this case. The oscillation frequency, f, is used to define the non-dimensional frequency, known as the Strouhal number, $St = \frac{fD}{U_g}$. The particle's oscillatory behavior is effectively captured, as presented in Fig. 3, which shows both the horizontal particle velocity and angular motion. In Table 3 we summarize the SEM and IBM results from MUD21 and compare our findings with theirs. In line with the results from the previous test case (Section 3.2.1), the simulations with volume-forcing tend to produce marginally higher settling velocities, u_{pV}, compared to the SEM reference data. For the deviations of the settling velocity and the horizontal velocity, we observe that the results converge towards the reference results. While all simulations exhibit some deviation from single-plane motion, our approach reveals a consistent convergence, especially in the high-resolution scenario, where the deviations from the single plane motion become minimal. This is evident from the absolute error of the amplitude of the $u_{pHz\perp}$-velocity reported directly in Table 3. Especially at higher resolutions, the amplitude of angular velocity, $\omega_{pHz\perp}$, and maximum tilting angle, ϕ_{max}, values are particularly convincing. In general, all the errors are reasonably low, of the same order as the IBM results presented in MUD21.

3.3. Rising spheroid in unbounded domain

In this section, we focus on the capability of the method to simulate the motion of light particles ($\tilde{\rho} < 1$). Hence, we analyze a single ascending spheroid in an unbounded domain and compare the results to the spectral element results of Zhou et al. (2017). Two regimes are considered: the steady-vertical and the vertical-periodic. The computational domain has almost the same dimensions as in the previous section with $L_x = L_y = 6D$ and $L_z = 18D$, as shown in Fig. 1d. The boundary conditions are adapted, hence, we impose a vertical velocity $\boldsymbol{u}(x, y, L_z) = -U_\infty \boldsymbol{e}_z$ at the top, where $\boldsymbol{U}_\infty$ is an estimation of the particle's settling velocity (see Section 3.2). We also apply an advective boundary condition at the bottom and enforce periodicity for the lateral boundaries. For this test case, we consider an aspect ratio $\chi = 2$, a density ratio of $\tilde{\rho} = 0.955$, and the following grid resolutions $D/\Delta x = 8$, 16, 32 and 64. This results in a grid size of $(384 \times 384 \times 1152)$ for the case with the highest resolution. The time step has been selected in all cases such that $CFL \approx 0.3$.

Table 3
Parameters and results for the vertical-periodic regime for a settling oblate spheroid. Reference data taken from Moriche et al. (2021). The corresponding SEM values are used for normalization (ϕ^*_{ref} in Eq. (49)), expect for $\varepsilon_{V'}$ and $\varepsilon_{H'}$, where we use $\phi^*_{ref} = u^{\mathrm{SEM}}_{p,V}$.

Method	Work	$\frac{D}{\Delta x}$	Forcing	St	ε_{St}	u_{pV}	ε_V	u'_{pV}	$\varepsilon_{V'}$	u'_{pH}	$\varepsilon_{H'}$	$u'_{pHz\perp}$	$\omega'_{pHz\perp}$	$\varepsilon_{\omega'}$	$\phi_{max}(^\circ)$	ε_ϕ
SEM	MUD21 (C15-M075-SEM)	–	–	0.1096	–	−1.099	–	0.0024	–	0.1225	–	0	0.225	–	9.3055	–
IBM	MUD21 (C15-M075-24)	21.0	Surface	0.1025	0.0645	−1.094	0.0045	0.0017	0.0006	0.1033	0.0184	0.0003	0.175	0.222	7.7616	0.1659
IBM	MUD21 (C15-M075-48)	42.0	Surface	0.1051	0.0411	−1.083	0.0146	0.0025	0.0002	0.1213	0.0011	0.0004	0.195	0.133	8.4161	0.0955
IBM	Current	21.0	Volume	0.1099	0.0027	−1.147	0.0436	0.0019	0.0004	0.1033	0.0175	0.0007	0.178	0.208	7.3984	0.2049
IBM	Current	42.0	Volume	0.1099	0.0027	−1.128	0.0263	0.0021	0.0002	0.1196	0.0026	0.0002	0.213	0.053	8.8523	0.0487

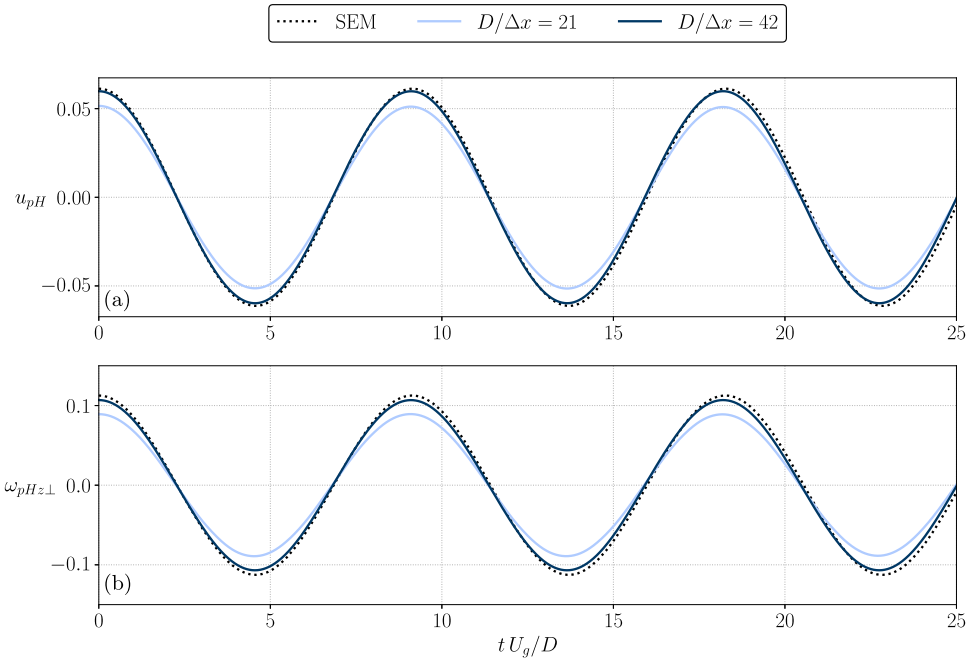

Fig. 3. Oscillatory dynamics for a settling oblate ($\chi = 1.5$) are compared. Figure showing (a) the horizontal velocity ratio, u_{pH}/U_g, and (b) the angular velocity, $\omega_{pHz\perp}$. The current deployed IBM with different resolutions ($D/\Delta = 21$ and 42) is compared against SEM reference data obtained by Moriche et al. (2021).

Table 4
Parameters and results for the steady-vertical regime for a rising oblate spheroid. Reference data from Zhou et al. (2017).

Method	$D/\Delta x$	u_{pV}	ε_V	$\langle \varepsilon(u_{r\parallel})^2 \rangle_z^{1/2}$
SEM	–	0.9053	–	–
IBM	8	0.8704	0.0386	0.0495
IBM	16	0.8907	0.0161	0.0152
IBM	32	0.8897	0.0172	0.0103
IBM	64	0.8870	0.0202	0.0096

3.3.1. Steady-vertical regime

We first consider the steady-vertical regime. In accordance with Zhou et al. (2017), we set the Galileo number to $Ga = 110.5$. In this regime, the spheroid rises while maintaining a stable orientation, with its symmetry axis aligned vertically. The regime is characterized by a constant vertical velocity without oscillations or tumbling. We observe that the proposed method is able to capture the steady-vertical regime for all resolutions considered (Fig. 4, Table 4). The present simulations converge to a somewhat lower value of the settling velocity compared to the reference data, with a difference of about 2% on the finer grids (Table 4).

Next, we compare the flow field at steady-state along the symmetry axis to the reference data. First, the relative velocity, $\mathbf{u}_r(\mathbf{x}, t) = (u_r, v_r, w_r) = \mathbf{u} - \mathbf{u}_p$, represents the relative motion between the fluid and particle. The axial component is defined as $u_{r\parallel} = w_r$ and the radial component as $u_{r\perp} = \sqrt{u_r^2 + v_r^2}$. The error of the axial component is defined as $\epsilon(u_{r\parallel}) = \left| u^{\mathrm{IBM}}_{r\parallel} - u^{\mathrm{SEM}}_{r\parallel} \right|$. Since in the reference flow the radial component is $u^{\mathrm{SEM}}_{r\perp} = 0$, $u_{r\perp}$ directly reflects the absolute error.

The present results for the relative motion along the symmetry axis are compared to the reference data in Fig. 4. For the axial relative velocity, $u_{r\parallel}$, we observe good agreement except for the low-resolution case ($D/\Delta x = 8$), where the error, particularly in the far-wake region, is significantly higher. A measure of this error is gathered in Table 4 to illustrate the convergence with the grid resolution. A similar trend is observed for the radial velocity (Fig. 4b), with good agreement near the particle as the resolution increases. Our findings indicate that the method effectively represents the steady-vertical regime; however, the results at a resolution of $D/\Delta x = 8$ suggest that this resolution is insufficient for an accurate representation of the flow.

3.3.2. Vertical-periodic regime

Finally, we consider the vertical-periodic regime for the rising oblate spheroid. Following Zhou et al. (2017), the Galileo number is set to $Ga = 166$. In this state, the spheroid has a primary ascending vertical movement, with periodic oscillations occurring solely within one plane. We use the same notation as in section Section 3.2.2. The results are gathered in Table 5 and the time evolution of two representative quantities, the lateral velocity and the angular velocity, is shown in Fig. 5. Both quantities show a good agreement with the reference data with increasing grid resolution, being the lateral velocity slightly overpredicted and the angular velocity slightly underpredicted. The comparison with the reference data in the table shows that the

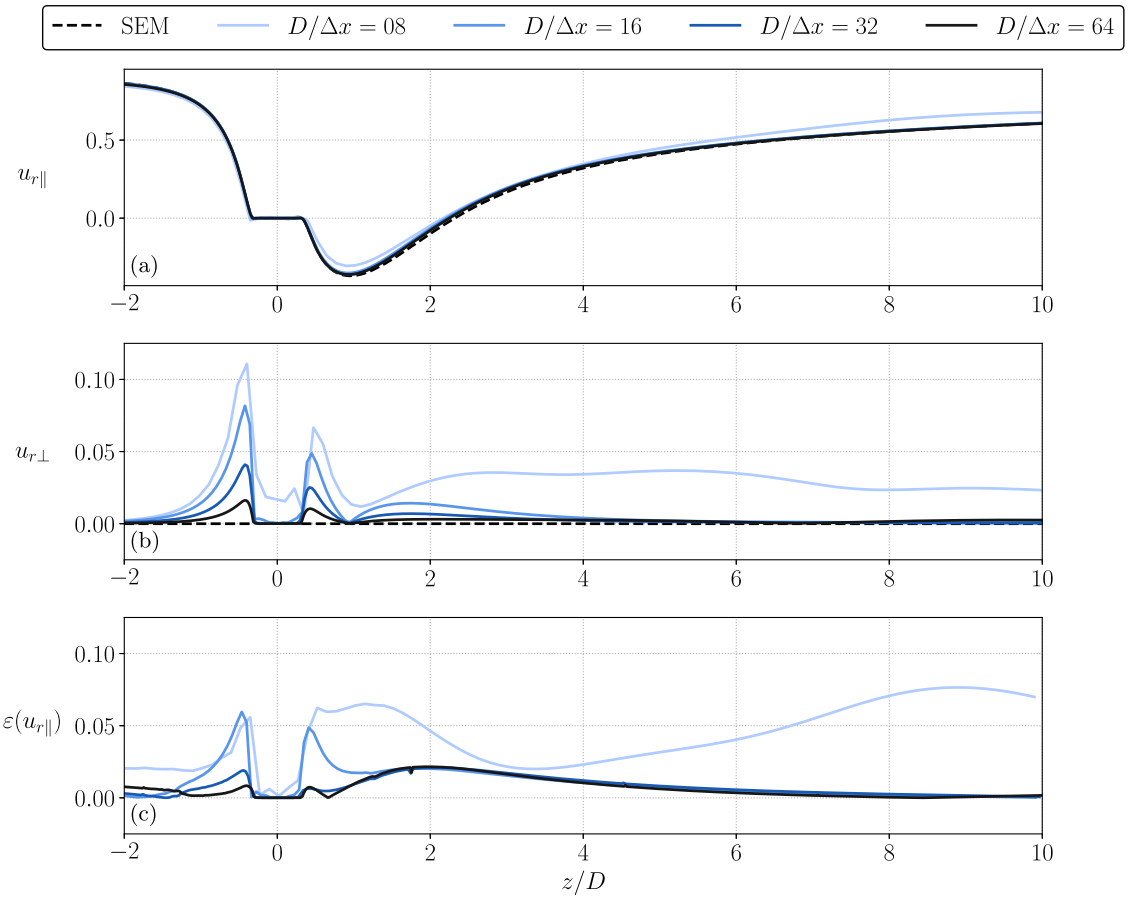

Fig. 4. Comparison of the relative motion between fluid and particle along the symmetry axis. The proposed IBM is evaluated against SEM reference data from Zhou et al. (2017) at multiple resolutions ($D/\Delta x = 8, 16, 32$ and 64). (a) shows the axial relative velocity $u_{r\parallel}$, (b) the radial relative velocity $u_{r\perp}$ and (c) shows the error, $\varepsilon(u_{r\parallel})$, of the axial component.

Table 5
Parameters and results for the vertical-periodic regime for a rising oblate spheroid. Reference data from Zhou et al. (2017). The corresponding SEM values are used for normalization (ϕ^*_{ref} in Eq. (49)), expect for $\varepsilon_{V'}$ and $\varepsilon_{H'}$, where we use $\phi^*_{ref} = u^{\mathrm{SEM}}_{p,V'}$.

Meth.	$\frac{D}{\Delta x}$	St	ε_{St}	u_{pV}	ε_V	u'_{pV}	$\varepsilon_{V'}$	u'_{pH}	$\varepsilon_{H'}$	$u'_{pHz\perp}$	$\omega'_{pHz\perp}$	$\varepsilon_{\omega'}$	$\phi_{max}(^\circ)$	ε_ϕ
SEM	–	0.0887	–	0.9102	–	0.0139	–	0.2251	–	0	0.2819	–	14.379	–
IBM	16	0.0867	0.0225	0.9336	0.0257	0.0164	0.0027	0.1623	0.0701	0.0394	0.1693	0.3994	09.703	0.3251
IBM	32	0.0892	0.0056	0.9103	0.0001	0.0104	0.0038	0.2011	0.0264	0.0002	0.2419	0.1418	12.229	0.1495
IBM	64	0.0895	0.0090	0.9012	0.0098	0.0112	0.0030	0.2114	0.0151	0.0001	0.2628	0.0677	13.282	0.0762

proposed method is able to capture the vertical-periodic regime accurately. All quantities converge with increasing grid resolution to values that are in reasonably good agreement with the reference data. Note also that the value of the velocity component perpendicular to the plane where the motion should be contained, $u_{pHz\perp}$, converges towards zero with increasing grid resolution. This indicates that indeed the method is able to capture the rising light spheroid in the regime with periodic oscillations contained in one plane. A snapshot of the wake of the rising spheroid is shown in Fig. 5c–d, visualized using an iso-surface of the second-invariant of the velocity-gradient tensor Q (Hunt et al., 1988), corresponding to the case with grid resolution $D/\Delta x = 32$. The visualization illustrates the double-threaded character of the structures in the wake (panel c) and the direction along which the periodic swaying of the structure occurs (panel d).

4. Conclusions

We have presented an efficient immersed boundary method to perform particle-resolved simulations of rigid particles of arbitrary shape.

This work represents an extension of the method proposed by García-Villalba et al. (2023) for spheres. The stability limitations remain the same in terms of the minimum density ratio that can be simulated ($\rho_p/\rho_f > 0.5$). Therefore, this is a disadvantage compared to the method of Tschisgale et al. (2018) where no limitation exists in terms of density ratio. The main advantage of the proposed methodology is its simplicity: no additional extra terms are needed in the particle equations and also there is no need to deal with the cross term that usually appears in the equation of the angular momentum of the particle. The simplicity of the formulation is particularly evident for the case of neutrally-buoyant particles.

The validation of the methodology has been performed using three test cases from the literature. First, a neutrally-buoyant prolate spheroid in a shear flow was studied. In this case, there is an analytical solution in the limit of Stokes flow. Here the computations have been performed at very low but finite Reynolds number, showing good agreement with the reference solution. As a second validation case, we have studied the settling of an oblate spheroid in ambient fluid. We have considered two challenging flow regimes: the steady-oblique regime and the vertical-periodic regime. We have compared results

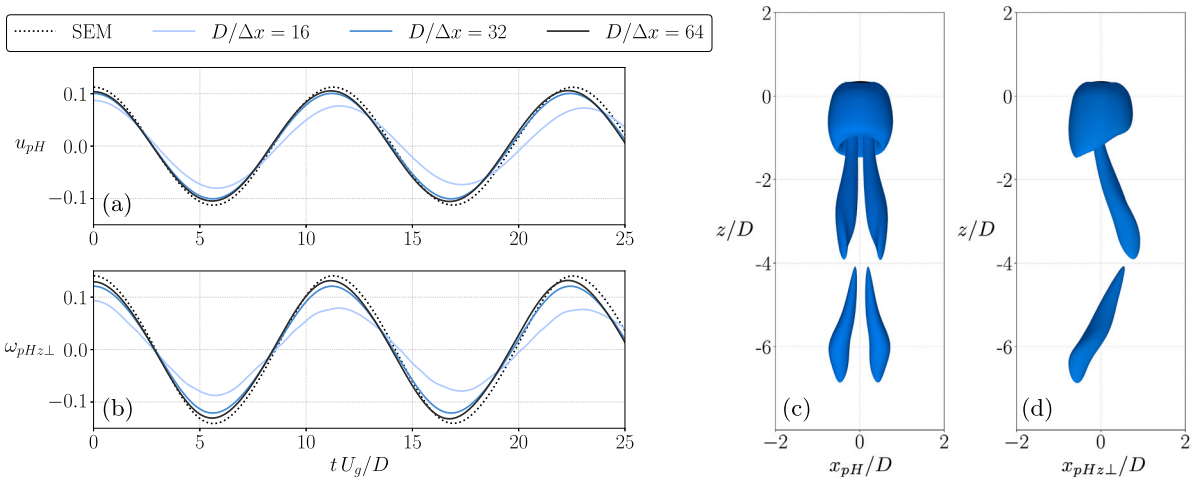

Fig. 5. Comparison of the oscillatory behavior of a rising spheroid. SEM reference data from Zhou et al. (2017) is evaluated against the proposed IBM at different resolutions ($D/\Delta x = 16, 32$ and 64), where (a) shows the horizontal velocity, u_{pH}/U_g, and (b) the angular velocity, $\omega_{pHz\perp}$. (c) and (d) Two views of an iso-surface of $Q = 0.1\,U_g^2/D^2$.

obtained using the proposed method with reference results obtained with a spectral/spectral-element method, and with the original version of Uhlmann's IBM extended for non-spherical objects. The results of the proposed method are in reasonably good agreement with the SEM results and are comparable to those of the original formulation. Finally, we have studied the case of a rising oblate spheroid, for which the original IBM formulation does not work for stability reasons. Again we have considered two regimes, the steady vertical regime and the vertical periodic regime, obtaining good agreement in both cases with respect to the reference results.

In summary, the study demonstrates that the proposed approach provides a simple, cost-efficient and accurate modification to the original method, enabling simulations of moderately light particles with arbitrary shapes. As a result, it is particularly well suited to the study of large-scale configurations with a large number of neutrally-buoyant particles.

CRediT authorship contribution statement

Maximilian Schenk: Writing – review & editing, Writing – original draft, Visualization, Validation, Software, Methodology, Data curation. **Manuel García-Villalba:** Writing – review & editing, Validation, Software, Project administration, Methodology, Investigation, Conceptualization. **Jan Dušek:** Writing – review & editing, Validation, Software, Methodology, Data curation. **Markus Uhlmann:** Writing – review & editing, Validation, Software, Methodology. **Manuel Moriche:** Writing – review & editing, Validation, Supervision, Software, Methodology, Investigation, Data curation, Conceptualization.

Declaration of competing interest

The authors declare that they have no known competing financial interests or personal relationships that could have appeared to influence the work reported in this paper.

Acknowledgments

The authors acknowledge TU Wien Bibliothek for financial support through its Open Access Funding Programme.

Appendix A. Rotation matrix

To track the particle's motion, we establish a relationship between the global reference frame and body-fixed reference frame, characterized by a rotation between these two. The spatial rotations between the two reference frames are conveniently described using a formulation based on quaternions, $\boldsymbol{q} = (q_1, q_2, q_3, q_4)$. Quaternions are characterized by a vector, $\boldsymbol{e}$, representing the rotation axis, and the rotating angle, φ, as $q_i = e_i \sin(\varphi/2)$ for $i = 1, 2, 3$ and $q_4 = \cos(\varphi/2)$. Following Tewari (2007), the quaternions evolve according to:

$$\frac{\mathrm{d}\boldsymbol{q}}{\mathrm{d}t} = \frac{1}{2}\boldsymbol{Q}\boldsymbol{q}, \tag{54}$$

where the matrix $\boldsymbol{Q}$ in terms of the angular velocity is defined by

$$\boldsymbol{Q} = \begin{pmatrix} 0 & \omega_{pz,b} & -\omega_{py,b} & \omega_{px,b} \\ -\omega_{pz,b} & 0 & \omega_{px,b} & \omega_{py,b} \\ \omega_{py,b} & -\omega_{px,b} & 0 & \omega_{pz,b} \\ -\omega_{px,b} & -\omega_{py,b} & -\omega_{pz,b} & 0 \end{pmatrix}. \tag{55}$$

The rotation matrix, $\mathcal{R}$, and its transpose, $\mathcal{R}^T$, allow a proper transformation between the body-fixed reference frame and the global reference frame ($\mathbf{y}_b = \mathcal{R}\mathbf{y}$) and vice versa ($\mathbf{y} = \mathcal{R}^T\mathbf{y}_b$). As described in Tewari (2007), the rotation matrix, $\mathcal{R}$, can be calculated from the quaternions as follows

$$\mathcal{R} = \begin{pmatrix} q_1^2 - q_2^2 - q_3^2 + q_4^2 & 2(q_1q_2 + q_3q_4) & 2(q_1q_3 - q_2q_4) \\ 2(q_1q_2 - q_3q_4) & -q_1^2 + q_2^2 - q_3^2 + q_4^2 & 2(q_2q_3 + q_1q_4) \\ 2(q_1q_3 + q_2q_4) & 2(q_2q_3 - q_1q_4) & -q_1^2 - q_2^2 + q_3^2 + q_4^2 \end{pmatrix}. \tag{56}$$

Appendix B. Computational cost associated to surface- and volume-forcing approaches

In this section we present an evaluation of the cost related to IBM operations and its impact on the total simulation cost, focusing on the differences between surface- and volume-forcing strategies. We have used a serial code capable of handling small to medium size simulations. The computations were performed using an Intel IceLake-6326 processor featuring 24 MB of L3 cache and a 2.9 GHz clock speed. We have conducted a test involving a settling sphere with density ratio $\tilde{\rho} = 1.5$ and Galileo number $Ga = 100$ in a cuboidal domain with lateral dimensions $L_x = L_y = 8D$ and height $L_z = 24D$. We select grid resolutions of $D/\Delta x = 16, 32$ and 64, resulting in grid sizes of ($128 \times 128 \times 384$), ($256 \times 256 \times 768$) and ($512 \times 512 \times 1536$), respectively. And similar to the benchmarks conducted in Sections 3.2 and 3.3, we impose an inflow/outflow configuration in the vertical direction and periodicity in the lateral directions. In this section we define t_{IBM} as the wall time per step spent in IBM-related computations (interpolation/spreading operations) averaged over 100 steps. We also define t_{total} as the total wall time per step (also averaged over 100 steps).

Table 6
Cost estimations for dilute and dense systems.

Volume fraction	Regime	$D/\Delta x$	$N_{b,i}$	N_L^{Surface}	N_L^{Volume}	r_i^{Surface}	r_i^{Volume}
$\phi_{ref} = 0.0341\%$	Reference	16	1	805	3053	0.089%	0.29%
$\phi_1 = 0.50\%$	Dilute	16	15	11 809	44 787	1.29%	4.14%
$\phi_2 = 10.0\%$	Dense	16	293	236 146	895 597	20.7%	46.4%
$\phi_{ref} = 0.0341\%$	Reference	32	1	3218	20 579	0.038%	0.20%
$\phi_1 = 0.50\%$	Dilute	32	15	47 208	301 893	0.56%	2.83%
$\phi_2 = 10.0\%$	Dense	32	293	944 000	6 036 849	10.0%	36.8%
$\phi_{ref} = 0.0341\%$	Reference	64	1	12 869	150 532	0.017%	0.17%
$\phi_1 = 0.50\%$	Dilute	64	15	188 788	2 208 304	0.25%	2.38%
$\phi_2 = 10.0\%$	Dense	64	293	3 775 121	44 158 562	4.7%	32.8%

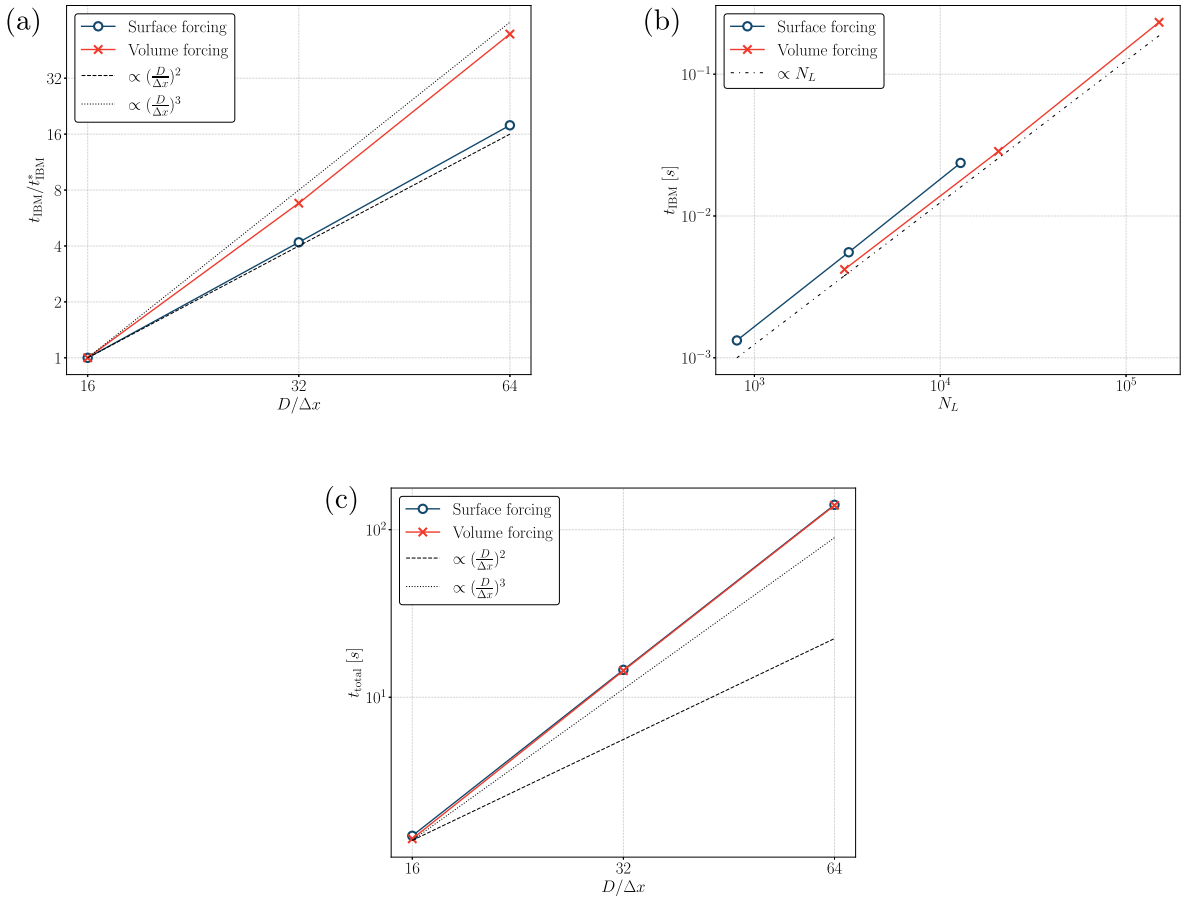

Fig. 6. Wall time measurements of IBM-related computations versus (a) spatial resolution and (b) number of Lagrangian markers. (c) Wall time measurement of the total time. t^*_{IBM} in panel (a) is the wall time for the case with lower resolution ($D/\Delta x = 16$) of the corresponding forcing approach (surface or volume).

According to the method of Uhlmann (2005) the number of markers, N_L, to discretize a particle is proportional to $\left(\frac{D}{\Delta x}\right)^2$ and $\left(\frac{D}{\Delta x}\right)^3$ for surface- and volume-forcing, respectively. Fig. 6a shows t_{IBM} normalized by its value at the lowest resolution vs $D/\Delta x$, where it can be seen that the cost of surface-forcing increases as $\propto \left(\frac{D}{\Delta x}\right)^2$, and the cost of volume-forcing as $\propto \left(\frac{D}{\Delta x}\right)^3$. Fig. 6b shows t_{IBM} as a function of N_L, where we see that the cost is proportional to N_L. Fig. 6c shows t_{total} as a function of $D/\Delta x$, showing that the total cost using both approaches is barely affected by the difference in cost of the IBM-related computations, since the latter is essentially negligible compared to the total cost. It could be argued that this is because we are studying a very dilute system consisting of just one particle. Therefore, it is interesting to estimate for which solid volume fractions the cost of the IBM-related operations becomes significant, and the savings in the interpolation step mentioned in Section 2 become an advantage in the proposed method. In the following we show an estimation of the impact of surface-/volume-forcing considering typical values of particle concentration observed in particle-laden flows to provide a broader perspective on the influence of IBM-related costs. We quantify the particle concentration with ϕ, the solid volume fraction. The value obtained for the computations with one particle (shown above) is $\phi_{ref} = 0.0341\%$ and the values used for the estimations are $\phi = 0.5\%$ and $\phi = 10\%$, corresponding to dilute and dense regimes, respectively. The number of bodies, $N_{b,i}$, required for the ith solid volume fraction considered are obtained from the definition of ϕ_i

$$\phi_i = N_{b,i} \underbrace{\frac{V_p}{V}}_{\phi_{ref}} \Rightarrow N_{b,i} = \frac{\phi_i}{\phi_{ref}}, \tag{57}$$

where V is the volume of the mixture (solid and fluid) and V_p is the volume of one particle. Assuming that the computational time for the fluid solver will not be affected by increasing solid volume fraction, we

compute its value from our results for a single particle

$$t_f = t_{\text{total}} - t_{\text{IBM}}\,, \tag{58}$$

and, hence, we can use it to extrapolate the total computational time needed for the ith solid volume fraction:

$$t_{\text{total},i} = t_f + t_{\text{IBM}} \cdot N_{b,i}\,. \tag{59}$$

Finally, we compute the ratio r_i to measure the impact of the IBM-related operations on the total cost

$$r_i = \frac{t_{\text{IBM}} \cdot N_{b,i}}{t_{\text{total},i}}\,. \tag{60}$$

Table 6 shows the results obtained and the estimated values for the dilute and dense regime. The results show that indeed volume-forcing is more expensive than surface-forcing. For dilute systems the cost is tolerable for both approaches. On the other hand, for dense systems the computational cost of IBM-related computations for both approaches may be significant, being clearly much higher in the case of volume-forcing.

Data availability

Data will be made available on request.

References

Arranz, G., Martínez-Muriel, C., Flores, O., García-Villalba, M., 2022. Fluid–structure interaction of multi-body systems: Methodology and applications. J. Fluids Struct. 110, 103519.

Breugem, W.P., 2012. A second-order accurate immersed boundary method for fully resolved simulations of particle-laden flows. J. Comput. Phys. 231, 4469–4498.

Brown, D.L., Cortez, R., Minion, M.L., 2001. Accurate projection methods for the incompressible Navier–Stokes Equations. J. Comput. Phys. 168, 464–499.

Chrust, M., Bouchet, G., Dušek, J., 2013. Numerical simulation of the dynamics of freely falling discs. Phys. Fluids 25.

García-Villalba, M., Fuentes, B., Dušek, J., Moriche, M., Uhlmann, M., 2023. An efficient method for particle-resolved simulations of neutrally buoyant spheres. Comput. & Fluids 263, 105936.

Griffith, B.E., Patankar, N.A., 2020. Immersed methods for fluid–structure interaction. Annu. Rev. Fluid Mech. 52, 421–448.

Guazzelli, E., Morris, J.F., Pic, S., 2012. A Physical Introduction To Suspension Dynamics. Cambridge University Press.

Hunt, J.C.R., Wray, A.A., Moin, P., 1988. Eddies, streams, and convergence zones in turbulent flows. In: Studying Turbulence using Numerical Simulation Databases, vol. 2, pp. 193–208.

Jeffery, G.B., 1922. The motion of ellipsoidal particles immersed in a viscous fluid. Proc. R. Soc. Lond 102 (161).

Kempe, T., Fröhlich, J., 2012. An improved immersed boundary method with direct forcing for the simulation of particle laden flows. J. Comput. Phys. 231, 3663–3684.

Lloyd, S., 1982. Least squares quantization in PCM. IEEE Trans. Inform. Theory 28, 129–137.

Mittal, R., Bhardwaj, R., 2021. Immersed boundary methods for thermofluids problems. Annu. Rev. Heat Transf. 24.

Mittal, R., Iaccarino, G., 2005. Immersed boundary methods. Annu. Rev. Fluid Mech. 37, 239–261.

Mittal, R., Seo, J.H., 2023. Origin and evolution of immersed boundary methods in computational fluid dynamics. Phys. Rev. Fluids 8, 100501.

Moriche, M., Uhlmann, M., Dušek, J., 2021. A single oblate spheroid settling in unbounded ambient fluid: A benchmark for simulations in steady and unsteady wake regimes. Int. J. Multiph. Flow 136, 103519.

Peskin, C.S., 1972. Flow patterns around heart valves: A numerical method. J. Comput. Phys. 10, 252–271.

Peskin, C.S., 2002. The immersed boundary method. Acta Numer. 11, 479–517.

Rai, M.M., Moin, P., 1991. Direct simulations of turbulent flow using finite-difference schemes. J. Comput. Phys. 96, 15–53.

Rettinger, C., Rüde, U., 2017. A comparative study of fluid-particle coupling methods for fully resolved lattice Boltzmann simulations. Comput. & Fluids 154, 74–89.

Roma, A.M., Peskin, C.S., Berger, M.J., 1999. An adaptive version of the immersed boundary method. J. Comput. Phys. 153, 509–534.

Schwarz, S., Kempe, T., Fröhlich, J., 2016. An immersed boundary method for the simulation of bubbles with varying shape. J. Comput. Phys. 315, 124–149.

Sotiropoulos, F., Yang, X., 2014. Immersed boundary methods for simulating fluid–structure interaction. Prog. Aerosp. Sc 65, 1–21.

Tewari, A., 2007. Atmospheric and Space Flight Dynamics : Modeling and Simulation with MATLAB and Simulink. Birkhäuser.

Tschisgale, S., Kempe, T., Fröhlich, J., 2017. A non-iterative immersed boundary method for spherical particles of arbitrary density ratio. J. Comput. Phys. 339, 432–452.

Tschisgale, S., Kempe, T., Fröhlich, J., 2018. A general implicit direct forcing immersed boundary method for rigid particles. Comput. & Fluids 170, 285–298.

Uhlmann, M., 2005. An immersed boundary method with direct forcing for the simulation of particulate flows. J. Comput. Phys. 209, 448–476.

Uhlmann, M., Derksen, J., Wachs, A., Wang, L.P., Moriche, M., 2023. Efficient methods for particle-resolved direct numerical simulation. In: Modeling Approaches and Computational Methods for Particle-Laden Turbulent Flows. Academic Press, pp. 147–184.

Uhlmann, M., Dusek, J., 2014. The motion of a single heavy sphere in ambient fluid: a benchmark for interface-resolved particulate flow simulations with significant relative velocities. Int. J. Multiph. Flow 59, 221–243.

Verzicco, R., 2023. Immersed boundary methods: Historical perspective and future outlook. Annu. Rev. Fluid Mech. 55, 129–155.

Yu, Z., Shao, X., 2007. A direct-forcing fictitious domain method for particulate flows. J. Comput. Phys. 227, 292–314.

Zhou, W., Chrust, M., Dušek, J., 2017. Path instabilities of oblate spheroids. J. Fluid Mech. 833, 445–468.